

# Symmetry restoration through chaotic hysteresis in a non-Hermitian optical trimer

Johanne Hizanidis<sup>1</sup> and Konstantinos G. Makris<sup>2,1</sup>

<sup>1</sup>*Institute of Electronic Structure and Laser, Foundation for Research and Technology-Hellas, 70013 Heraklion, Greece*

<sup>2</sup>*ITCP–Department of Physics, University of Crete, Heraklion, Greece*

(Dated: 29 May 2026)

We investigate symmetry restoration and spatially localized dynamics in a non-Hermitian optical trimer composed of three lossy waveguides with complex-valued couplings. Extending our previous analysis of the system’s global bifurcation structure, we adopt a site-resolved perspective in order to uncover how collective nonlinear dynamics emerge and reorganize across the individual waveguides. We show that the transition from asymmetric to symmetric states is mediated by a chaotic hysteretic regime involving the coexistence of asymmetric, periodic-symmetric, and chaotic-symmetric attractors. Within this regime, chaotic dynamics become spatially localized predominantly at the edge waveguides, while the central waveguide retains partial spectral coherence. Following symmetry restoration, the system develops multifrequency dynamics through a spatial period-doubling process, where the middle waveguide oscillates at twice the dominant frequency of the edge sites. These results reveal how Kerr nonlinearity and complex coupling organize symmetry restoration, chaos localization, and frequency differentiation in minimal non-Hermitian photonic lattices.

**Non-Hermitian photonic systems provide a versatile setting for exploring nonlinear dynamics in the presence of Kerr nonlinearity, dissipation, and complex-valued coupling. Their ability to support controllable gain, loss, and coupling mechanisms has established non-Hermitian photonics as an important platform for studying complex dynamics in optical waveguides and photonic lattices. Previous works on the optical trimer considered here focused on the global evolution of the total optical power and revealed intricate bifurcation sequences and fractal-like chaotic structures associated with the interplay between nonlinearity and the combined dissipation and complex coupling. In the present study, we demonstrate that a waveguide-resolved description uncovers an additional level of dynamical organization hidden in the global observables. In particular, the transition from asymmetric to symmetric dynamics is accompanied by the emergence of spatially localized chaos and multifrequency oscillatory behavior involving distinct dynamical roles for the edge and central waveguides. These findings highlight how even minimal dissipative photonic lattices can support rich dynamics and suggest that larger non-Hermitian systems may exhibit even more complex forms of chaos localization, multifrequency synchronization, and symmetry-breaking phenomena.**

dynamics and novel spectral properties beyond the constraints of conservative systems<sup>1–3</sup>. Their ability to support complex-valued coupling and dissipative nonlinear interactions has enabled the observation of exceptional points, unidirectional transport, and PT-symmetry breaking in compact optical configurations<sup>4–14</sup>. Among the simplest realizations are coupled-waveguide arrays, where light propagates through evanescently linked channels and the interplay between nonlinearity, loss, and coupling gives rise to rich nonlinear behavior, including multistability, self-trapping, and chaos<sup>15–19</sup>.

Within this framework, the so-called *actively coupled* (AC) dimer<sup>20</sup> composed of two lossy waveguides with gain distributed in the coupling, has served as a structurally stable alternative to the PT-symmetric case, where gain and loss must be equal. Extending this concept, the AC trimer introduced in Ref.<sup>21</sup> provides a natural next step toward understanding collective dynamics in small non-Hermitian photonic lattices. Despite its simplicity, this system supports an exceptionally rich variety of behaviors. The analysis in Ref.<sup>21</sup> focused on the global response of the trimer through the evolution of the total optical power. That study revealed a rich bifurcation structure involving analytically obtained stationary states, coexistence of symmetric limit cycles, and period-doubling routes to chaos accompanied by fractal-like organization in parameter space, while the underlying bifurcations were confirmed through continuation methods.

In the present work, we extend this study by focusing on the *site-resolved dynamics* of the trimer, aiming to uncover how the collective behavior manifests at the level of individual waveguides. This perspective allows us to explore the mechanisms through which symmetry breaking and restoration occur locally. In this context, symmetry denotes the invariance of the trimer under interchange of the two edge waveguides. A state is (a)symmetric when the outer waveguides exhibit (non)identical dynam-

## I. INTRODUCTION

Non-Hermitian photonic systems, characterized by spatially structured gain and loss, have emerged as versatile platforms for exploring unconventional optical dy-

ics and optical intensities. This framework further allows us to identify distinct dynamical regimes, including asymmetric oscillations, multifrequency synchronization, and chaos localization. Special attention is devoted to the transition from asymmetric to symmetric states, which proceeds through a regime of chaotic hysteresis involving the coexistence of multiple attractors. Understanding how such transitions arise in minimal non-Hermitian configurations provides valuable insight into the organization of nonlinear dynamics in larger photonic networks and coupled oscillator systems.

The paper is organized as follows. In Sec. II, we outline the non-Hermitian trimer model and briefly summarize the main findings of Ref.<sup>21</sup>, which analyzed its global bifurcation structure in terms of the total optical power. We then adopt a site-resolved perspective to examine the local dynamical features of each waveguide, highlighting the transition from asymmetric to symmetric behavior. Section III quantifies the observed transition and discusses the emergence of multifrequency and chaos-localized dynamical regimes. In Sec. IV, we investigate the mechanisms underlying these transitions, focusing on the role of chaotic hysteresis in symmetry restoration. Finally, in the conclusions we summarize the main results and outlines possible extensions of the present work.

## II. SITE-RESOLVED DYNAMICS

The model employed in this work was introduced in Ref.<sup>21</sup> as a spatial extension of the actively coupled dimer presented in<sup>20</sup>. It represents a minimal non-Hermitian optical configuration, consisting of three evanescently coupled, identical waveguides with complex-valued couplings and uniform loss. The coupling between adjacent sites is complex, with a real part  $k > 0$  and an imaginary part  $\alpha > 0$ , while each waveguide experiences a uniform loss rate  $\gamma > 0$ . Within the framework of coupled-mode theory<sup>22</sup>, the evolution of the optical field envelopes is governed by the following set of nonlinear equations:

$$\frac{d\psi_1}{dz} = -\gamma\psi_1 + (ik + \alpha)\psi_2 + i|\psi_1|^2\psi_1, \quad (1)$$

$$\frac{d\psi_2}{dz} = -\gamma\psi_2 + (ik + \alpha)(\psi_1 + \psi_3) + i|\psi_2|^2\psi_2, \quad (2)$$

$$\frac{d\psi_3}{dz} = -\gamma\psi_3 + (ik + \alpha)\psi_2 + i|\psi_3|^2\psi_3, \quad (3)$$

where  $\psi_j$  ( $j = 1, 2, 3$ ) denote the complex amplitudes of the optical fields and  $z$  is the propagation distance. Here,  $k$  is the linear coupling coefficient, while  $\alpha$ , which represents the symmetrically distributed gain, together with  $\gamma$ , introduce the non-Hermiticity of the model. Because of these terms, the corresponding linear problem is no longer energy conserving and the total optical power,  $P(z) = |\psi_1|^2 + |\psi_2|^2 + |\psi_3|^2$ , unlike in the Hermitian case, now depends on the propagation distance  $z$ .

In Ref.<sup>21</sup>, we investigated the dynamical behavior of this trimer model from a global perspective, focusing on the collective evolution of the total optical power. That study demonstrated that the system supports analytically tractable stationary states, whose stability and bifurcations were analyzed as functions of the loss rate and the complex coupling parameters. In the oscillatory regime, a sequence of bubble formations and period-doubling bifurcations was identified, eventually leading to chaotic dynamics. The calculation of the maximum Lyapunov exponent across the gain-loss parameter plane revealed a highly intricate arrangement of alternating regular and chaotic regions, exhibiting a fractal-like organization of the system's dynamics.

In the present work, our focus shifts from the global response of the system to the site-resolved dynamics, aiming to uncover how the collective behavior manifests locally in each waveguide. This more spatially detailed perspective allows us to probe the distribution and evolution of dynamical features across the trimer, especially in the lower- $\alpha$  region. The remaining parameters will be kept fixed at values  $k = 0.2$  and  $\gamma = 1.5$  throughout the whole paper, along the lines of<sup>21</sup>.

In this context, Fig. 1 displays the local maxima of the individual waveguide intensities as a function of the control parameter  $\alpha$ . The data shown here are obtained via numerical continuation, where each simulation uses the final state of the previous run as its initial condition. Very small maxima close to zero have been discarded to improve visibility. The vertical dashed lines mark four characteristic values of  $\alpha$ , labeled I-IV, which correspond to representative dynamical regimes that are examined in detail throughout this work.

Point I corresponds to an *asymmetric state*, characterized by an imbalance between the two edge waveguides: one maintains a higher intensity, while the other remains at a lower level. This state coexists with its mirror image and, as reported in<sup>21</sup>, emerges from a pitchfork bifurcation at lower  $\alpha$  and subsequently loses stability through a Hopf bifurcation, that produces periodic oscillations whose maxima are displayed in this figure.

Just below point II, the two edge-waveguide branches ( $P_1$  and  $P_3$ ) begin to merge: their maxima cross irregularly, indicating a narrow *chaotic regime* where the previously distinct asymmetric states mix. This chaotic behavior is followed by a periodic branch and a subsequent "bubble", below point III, where, as marked by the blue arrow in panel (b), the middle waveguide ( $P_2$ ) develops a clear *period-2 oscillation* while the edge waveguides remain in a period-1 state. This transition can be interpreted as a form of *spatial period-doubling*, where neighboring sites oscillate with distinct temporal periodicities within the same global dynamical regime.

Finally, at point IV, the two edge waveguides recover identical amplitudes, corresponding to a *symmetric state*. Throughout this sequence, the middle waveguide follows the dynamics of the initially higher-intensity edge waveguide, typically at slightly higher intensity values. Inter-

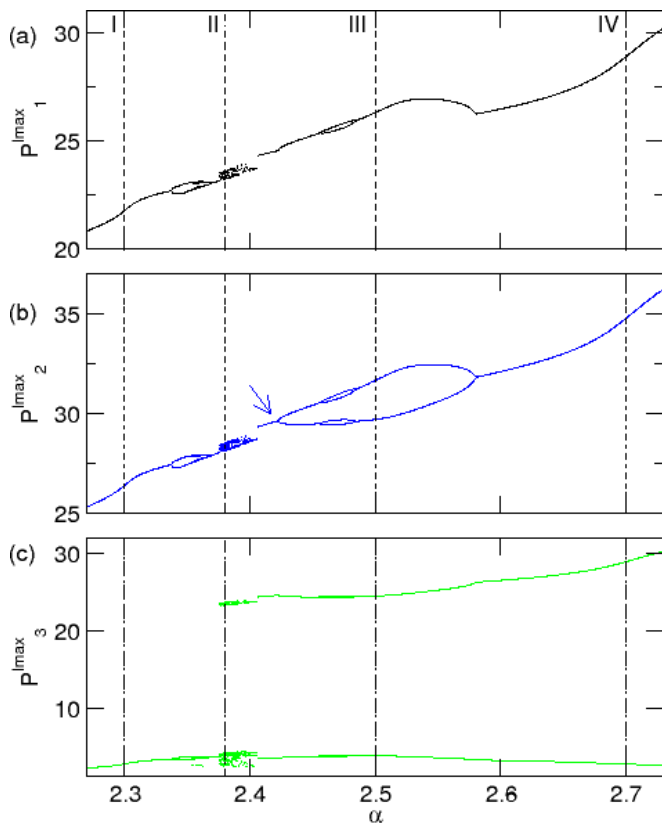


FIG. 1. Local maxima of the individual waveguide intensities as the parameter  $\alpha$  is varied: (a)  $P_1$  (black), (b)  $P_2$  (blue), and (c)  $P_3$  (green). The vertical dashed lines mark four representative values of  $\alpha$ , labeled I–IV, which correspond to characteristic dynamical regimes analyzed in Figs. 3 and 4. The blue arrow in (b) indicates the onset of a *period-2* oscillation in the middle waveguide, while the edge waveguides remain in a *period-1* state, an instance of a spatial period-doubling transition.

Interestingly, in the chaotic region the middle waveguide appears somewhat less disordered, a feature that will be discussed in detail later.

### III. MULTIFREQUENCY BEHAVIOR AND CHAOS LOCALIZATION

In order to quantify the degree of asymmetry between the edge waveguides, we compute the difference between their global maxima for random initial conditions at each value of  $\alpha$ , normalized to the larger of the two:

$$\Delta P_{13} = \frac{P_1^{\text{gmax}} - P_3^{\text{gmax}}}{\max(P_1^{\text{gmax}}, P_3^{\text{gmax}})}. \quad (4)$$

Here,  $P_i^{\text{gmax}}$  denotes the global maximum of the intensity in waveguide  $i$ , in contrast to the local maxima shown in Fig. 1. Figure 2(a) shows  $\Delta P_{13}$  as a function of  $\alpha$ . Values of  $\Delta P_{13}$  close to  $\pm 1$  correspond to *asymmetric states*, whereas values near zero indicate *symmetric edge states*.

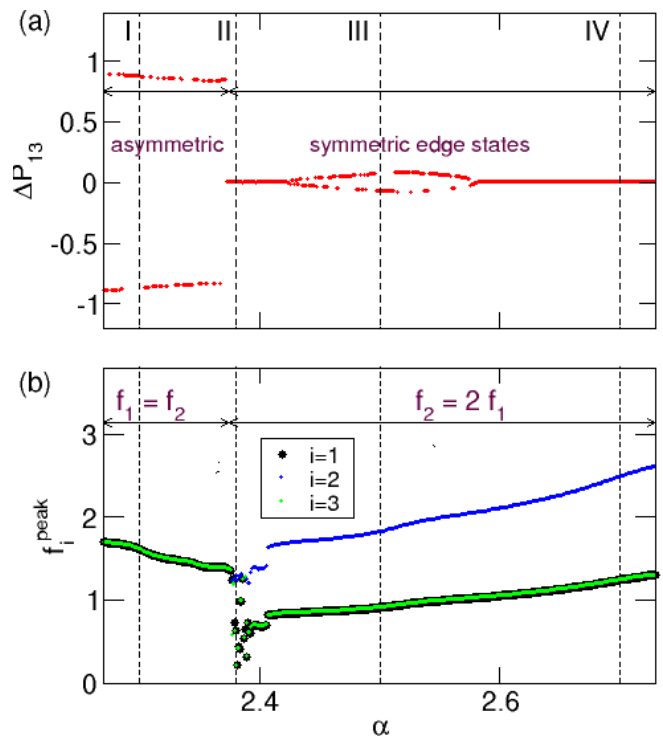


FIG. 2. Difference  $\Delta P_{13}$  between  $P_1$  and  $P_3$ , normalized to their maximum value, for random initial conditions at each point. (b) Frequency of the dominant peak in the power spectrum for all waveguides. Both quantities are shown as functions of the control parameter  $\alpha$ .

A sharp transition between the two regimes occurs just before point II, consistent with the behavior observed in Fig. 1. This transition marks the loss of asymmetry and the onset of near-amplitude-synchronous dynamics between the two edge waveguides.

Panel (b) of Fig. 2 presents the corresponding dominant frequencies,  $f_i^{\text{peak}}$ , extracted from the power spectra of all three waveguides. The edge waveguides ( $i = 1, 3$ ) maintain the same frequency across most of the parameter range, apart from the narrow chaotic region around point II, where the spectra become irregular. Within the asymmetric regime (region I), all three waveguides are frequency synchronized, indicating that the observed intensity imbalance arises from amplitude asymmetry rather than frequency detuning. When the system transitions to the symmetric regime, however, the middle waveguide ( $i = 2$ ) acquires a dominant spectral peak at approximately twice the frequency of the edge waveguides ( $f_2 \simeq 2f_1$ ). This frequency doubling persists throughout regions III and IV.

Although this behavior does not constitute a full chimera state in the strict sense since the coupling scheme is not global, it bears resemblance to a *small-frequency chimera*<sup>23</sup>, where a subset of oscillators (in this case, the middle waveguide) oscillates coherently yet with a distinct characteristic frequency compared to the otherwise synchronized ensemble.

The quantitative indicators introduced above are complemented by a direct visualization of the propagation dynamics and corresponding spectra, from which these measures are obtained. Figure 3 displays the intensity evolution  $P_i$  ( $i = 1, 2, 3$ ) in each waveguide (left panels) together with the corresponding Fourier power spectra  $S(f)$  (right panels) for the four representative cases I-IV indicated in Fig. 1.

The Fourier power spectrum of the intensity  $P_i(z)$  in the  $i$ th waveguide is defined as

$$S_i(f) = \left| \int_{-\infty}^{+\infty} P_i(z) e^{-i2\pi fz} dz \right|^2, \quad (5)$$

where  $f$  is the spatial frequency along the propagation coordinate  $z$ . Note that the spectra are vertically shifted for visual clarity.

Case I corresponds to the asymmetric state. The black and green traces represent the edge waveguides, which oscillate periodically and in antiphase: when  $P_1$  reaches its maximum,  $P_3$  attains its minimum, and vice versa. Both waveguides oscillate with the same frequency, as confirmed by the single dominant peak in their power spectra on the right. The middle waveguide (blue) follows the dynamics of the first edge waveguide, remaining nearly synchronized in frequency but at a slightly higher intensity level.

Case II lies within the chaotic regime. As seen in Fig. 2(a), the asymmetry between the edge waveguides vanishes ( $\Delta P_{13} \approx 0$ ), indicating a restoration of spatial symmetry. Here, for clarity, only the right-edge (3rd) waveguide is shown. The first one displays a similar chaotic fluctuation but with an opposite phase, that is, whenever  $P_3$  is high,  $P_1$  is low, and vice versa. Interestingly, the middle waveguide retains some degree of organization: its power spectrum exhibits weak but discernible peaks, whereas the edge waveguide displays a broad, continuous spectrum typical of fully developed chaos. This suggests a form of *spatial chaos localization*, where chaotic dynamics are preferentially confined to the outer sites while the central one remains more structured.

Spatial localization of nonlinear dynamics is well known in conservative lattice systems, where it can arise in the form of intrinsic localized modes, discrete breathers, and spatially confined chaotic states<sup>24,25</sup>. The present results demonstrate that related forms of chaos localization may also emerge in dissipative non-Hermitian photonic lattices, where complex-valued coupling and loss selectively redistribute chaotic activity across the system. The subsequent dynamical regime reveals that the restoration of symmetry is followed by the emergence of a qualitatively different form of organized oscillatory behavior.

Following this chaotic regime, case III corresponds to a symmetric state in which the middle waveguide exhibits a period-2 oscillation. To emphasize this feature, the corresponding power spectra are plotted on a different vertical scale. The spectrum of the middle waveguide displays an additional peak at half the main frequency

(marked by the blue arrow), which is characteristic of period-doubling behavior. At the same time, the small difference between the global maxima of the edge waveguides ( $P_1^{\text{gmax}}$  and  $P_3^{\text{gmax}}$ ), also evident in Fig. 2(a), is consistent with the weak residual asymmetry of this state.

Finally, case IV represents a fully symmetric periodic state. The intensities of the edge waveguides coincide perfectly in amplitude, and the middle waveguide exhibits a clear frequency doubling relative to them. This is reflected in the power spectra, where the dominant peak of the middle waveguide appears at twice the frequency of the edge modes ( $f_2 = 2f_1$ ), confirming the persistence of the frequency-doubled dynamics already identified in Fig. 2(b).

The four dynamical regimes presented in Fig. 3 are illustrated in a three-dimensional representation in Fig. 4. These spatially extended plots illustrate the intensity evolution  $P_i(z)$  across all waveguides, allowing a direct comparison of their relative amplitudes and phases. The asymmetric, chaotic, and frequency-doubled behaviors identified earlier become particularly clear here in the spatial domain: the antiphase oscillation of the edge waveguides in case I, the irregular fluctuations confined to the edges in case II, the alternating pattern of the middle waveguide in the period-2 state (case III), and the perfectly symmetric yet frequency-doubled oscillation of the middle site in case IV. This representation highlights the spatial structure of the observed transitions and complements the propagation and spectral analysis presented in Fig. 3.

#### IV. SYMMETRY RESTORATION VIA CHAOTIC HYSTERESIS

Having characterized and quantified the observed dynamical regimes, we now turn to a deeper analysis aimed at understanding the origin and nature of these transitions. Figure 5 elucidates the transition from asymmetric to symmetric states by showing the global maxima of  $P_1^{\text{gmax}}$  as the control parameter  $\alpha$  is varied. Black points correspond to the upswEEP and cyan points to the downswEEP, and the same color code is used in the phase portraits shown in the insets. A clear hysteretic behavior is observed, revealing the coexistence of multiple attractors and the sequence of symmetry-restoring transitions.

Region A corresponds to the asymmetric states, where the upswEEP and downswEEP branches coincide. Two mirror-related asymmetric solutions coexist, shown in the insets (a1) and (a2). In (a1) the first waveguide ( $P_1$ ) has high intensity while the third ( $P_3$ ) is low, and the opposite occurs in (a2). The dynamics in this regime is strictly periodic, with no indication of chaos.

As  $\alpha$  increases, the system enters the first hysteretic loop, denoted as region B. Here, the asymmetric solution corresponding to the upswEEP (black branch) remains regular and loses stability through a *saddle-node bifurcation of limit cycles* at a higher value of  $\alpha$  than the

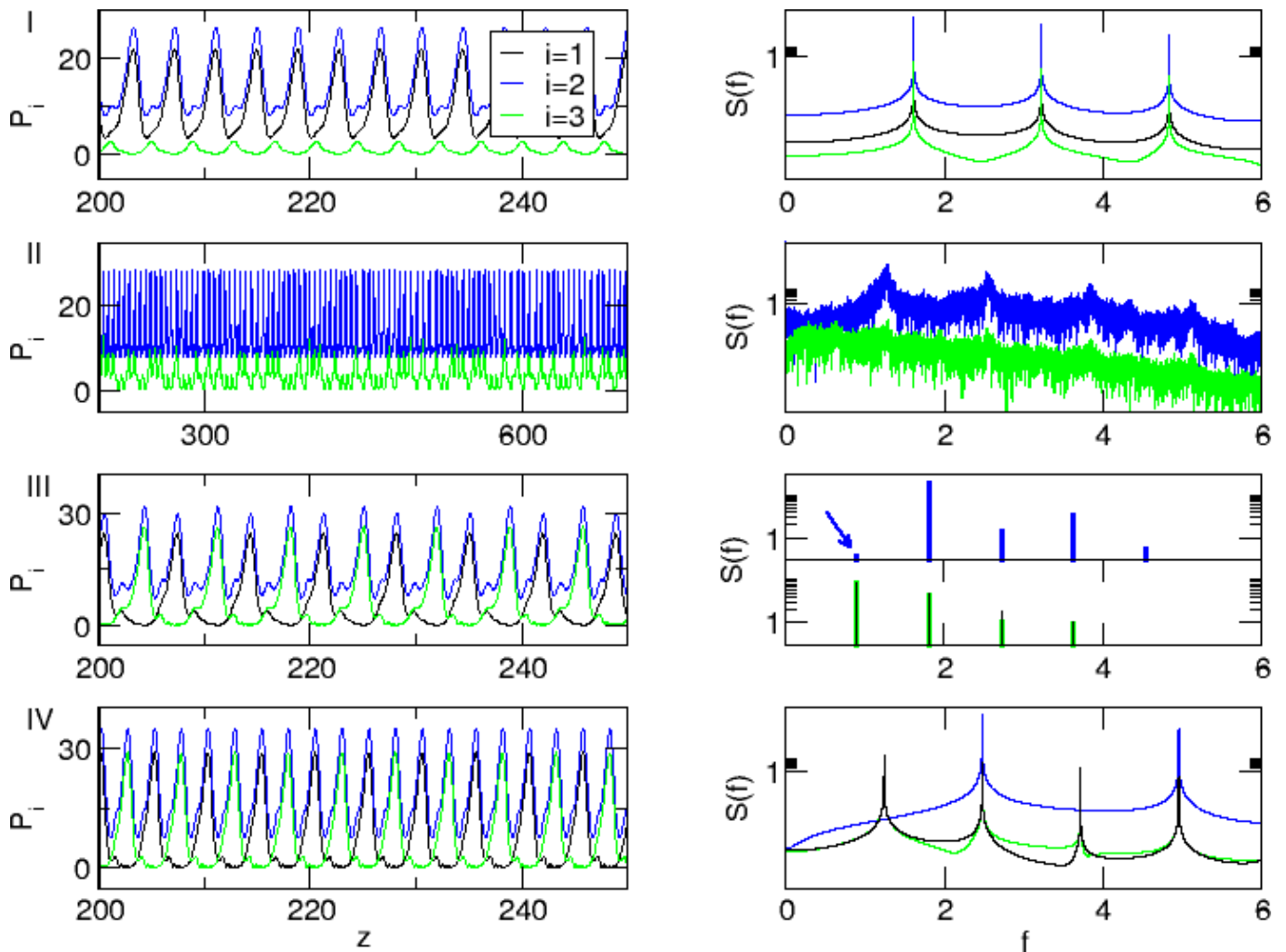


FIG. 3. Intensity  $P_i$  ( $i = 1, 2, 3$ ) in each waveguide (left) and the corresponding Fourier power spectra (right) for regions I–IV of Fig. 1. The power spectra  $S(f)$  are vertically shifted for better visualization in cases I, II, and IV. In case III, the spectra are plotted over a different vertical (power spectral density) range to highlight the small peak corresponding to the period-2 solution in the second waveguide, indicated by the blue arrow.

symmetric one (cyan branch), giving rise to the observed hysteresis loop. After the disappearance of the asymmetric orbit, the system follows the symmetric branch, which undergoes a transition to chaos as shown in <sup>21</sup>. The symmetric dynamics within this loop include the periodic orbit shown in (b2) and the chaotic symmetric state in (b3). The chaoticity was verified through the computation of the maximal Lyapunov exponent, which alternated between positive and zero values, an indicator of *intermittent chaos*. Thus, region B represents a symmetry-restoring process that occurs through a hysteretic and intermittently chaotic route, where symmetric and asymmetric solutions coexist.

Region C corresponds to the second hysteretic loop, where bistability persists but now between two *symmetric* periodic solutions, illustrated in the insets (c1) and (c2). The two branches are almost identical, differing only slightly in amplitude-differences that were already

visible in the  $\Delta P_{13}$  curve of Fig. 2(a).

Finally, in region D the upsweep and downsweep branches merge again, indicating the disappearance of bistability and the recovery of monostability with a single symmetric solution, as shown in the inset (d). This final state marks the completion of the transition from asymmetric to symmetric dynamics.

Similar transitions between symmetry-broken and symmetry-restored states have been reported in other nonlinear optical systems with inherent symmetries, such as the polarization-symmetric bistable model<sup>26</sup>, where asymmetric chaotic attractors undergo crisis-induced restructuring and eventually merge into statistically symmetric chaotic states. More broadly, chaotic hysteresis has also been investigated in externally driven nonlinear circuits<sup>27</sup>. In contrast, the hysteretic behavior observed in the present non-Hermitian trimer emerges intrinsically through the interplay between Kerr nonlinear-

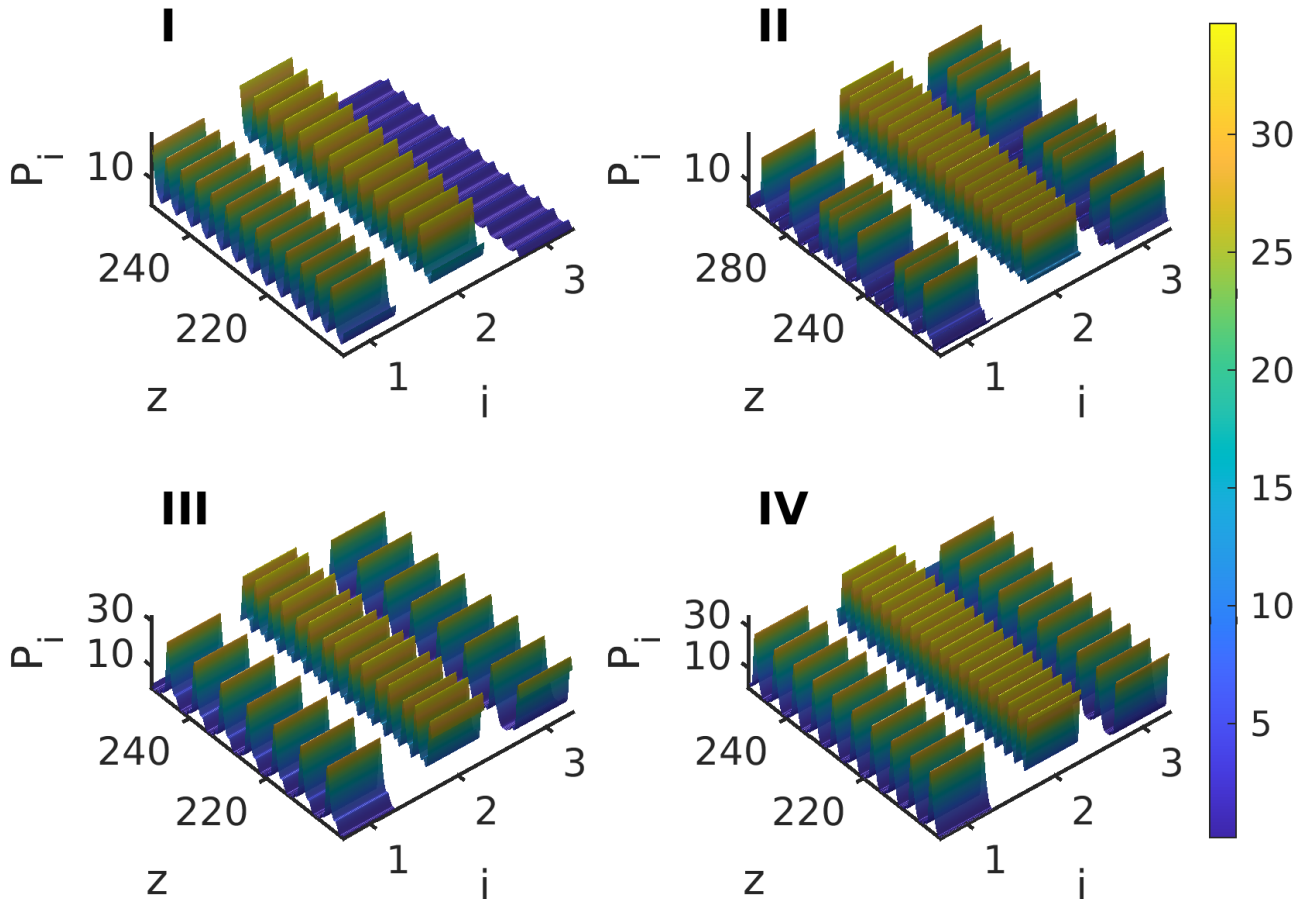


FIG. 4. Three-dimensional representations of the intensities  $P_i$  ( $i = 1, 2, 3$ ) in all waveguides for the points I-IV of Fig. 1. The spatially extended view allows visualization of all waveguides side by side: (I) asymmetric stationary state where all waveguides oscillate at the same frequency, (II) symmetric chaotic state with chaos localized in the edge waveguides, (III) symmetric state where the middle waveguide exhibits a period-2 oscillation, and (IV) symmetric periodic state in which the middle waveguide oscillates at twice the frequency of the edge waveguides.

ity, complex-valued coupling, and dissipation, without external forcing.

## V. CONCLUSIONS

In this work, we have examined the nonlinear dynamics of a non-Hermitian optical trimer with complex-valued couplings, extending our previous analysis of its global bifurcation structure to a site-resolved framework. By tracing the evolution of the individual waveguide intensities, we revealed how the collective behavior of the trimer manifests locally across the system.

The study identified a rich sequence of dynamical regimes, ranging from asymmetric oscillations and spatially localized chaos to multifrequency symmetric states. In particular, the transition from asymmetric to symmetric

behavior was shown to proceed through a hysteretic route involving the coexistence of periodic and chaotic attractors. Within this regime, the edge waveguides exhibit localized chaotic dynamics, while the middle one remains more regular and eventually develops frequency doubling-features reminiscent of a small-scale chimera state. This coexistence of localized and collective behavior highlights the subtle interplay between Kerr nonlinearity, gain-loss imbalance, and complex coupling in minimal non-Hermitian lattices.

Beyond clarifying the mechanisms of symmetry restoration and chaos localization in this archetypal three-site system, the present results may also provide insight into the dynamics of larger non-Hermitian arrays and other classes of nonlinear coupled oscillators where multistability, dissipation, and various coupling schemes coexist. In particular, similar mechanisms may arise in

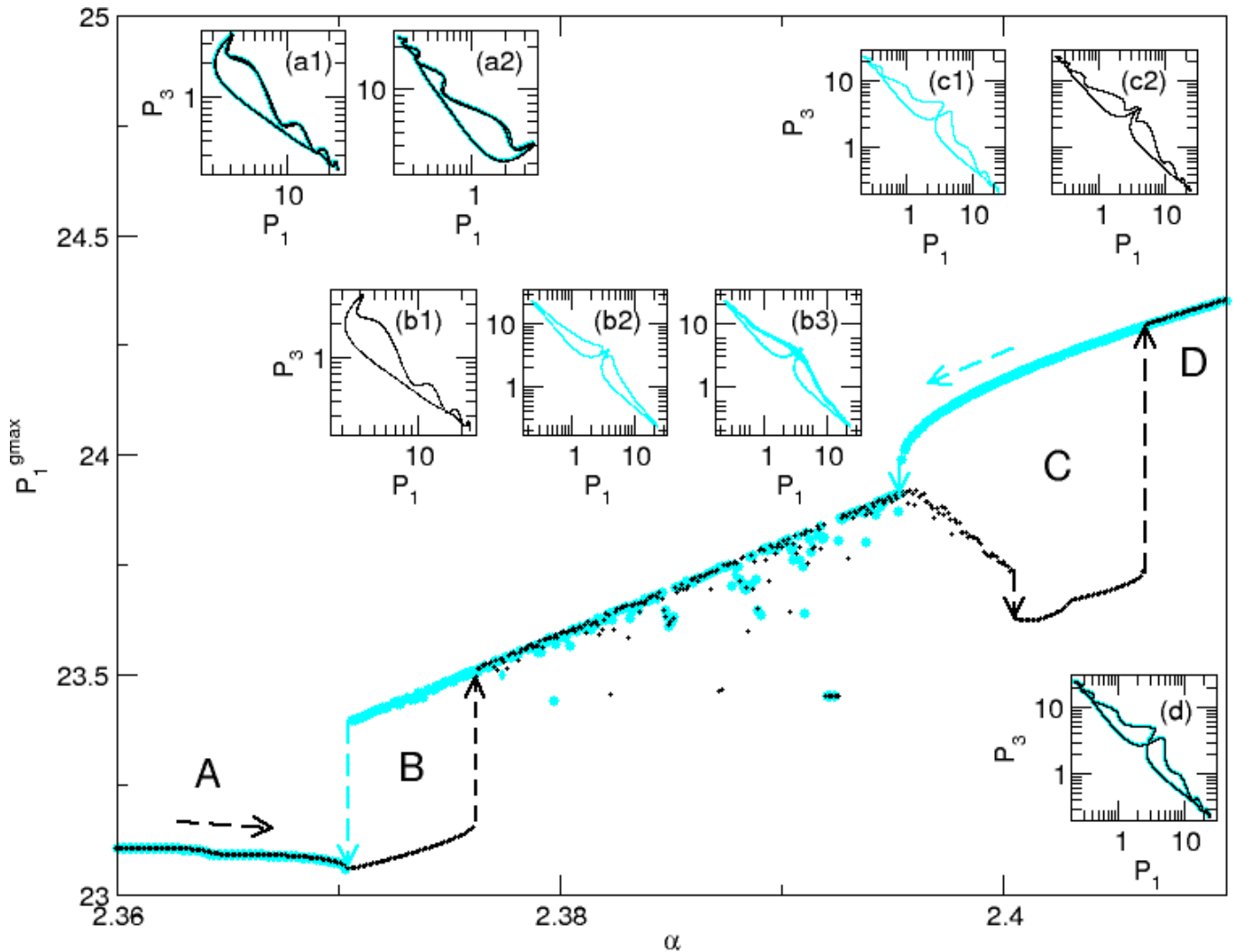


FIG. 5. Global maxima of  $P_1$  as the control parameter  $\alpha$  is varied. Black points correspond to the up-sweep and cyan points to the down-sweep. A transition is observed from asymmetric states (region A) to symmetric states (regions C and D) through a chaotic hysteretic regime (region B). The characteristic solutions of each region are illustrated in the corresponding phase portraits shown in the insets: (a1)–(a2) depict the coexisting asymmetric solutions of region A, (b1)–(b3) the coexisting asymmetric, periodic-symmetric, and chaotic-symmetric states of region B, (c1)–(c2) the coexisting periodic-symmetric solutions of region C, and (d) the single symmetric solution of region D. The same color code is used in the phase portraits, where black (cyan) orbits correspond to the up(down)sweep.

extended photonic lattices<sup>28</sup> and other related nonlinear oscillator arrays with significant technological relevance, supporting collective synchronization, pattern formation, and chaotic dynamics<sup>29</sup>. Future work may therefore explore how parameter inhomogeneity, higher-order couplings, and larger network topologies influence the emergence of chaotic hysteresis, localized chaoticity, and multifrequency synchronization in such systems.

#### ACKNOWLEDGMENTS

This project was funded by the European Research Council (ERC–Consolidator) under Grant Agreement

No. 101045135 (*Beyond Anderson*).

#### DATA AVAILABILITY STATEMENT

The data that support the findings of this study are available from the corresponding author upon reasonable request.

<sup>1</sup>R. El-Ganainy, K. G. Makris, M. Khajavikhan, Z. H. Musslimani, S. Rotter, and D. N. Christodoulides, *Nature Physics* **14**, 11 (2018).

<sup>2</sup>H. Hodaei, A. U. Hassan, S. Wittek, H. Garcia-Gracia, R. El-Ganainy, D. N. Christodoulides, and M. Khajavikhan, *Nature* **548**, 187 (2017).

- <sup>3</sup>M. P. Hokmabadi, A. Schumer, D. N. Christodoulides, and M. Khajavikhan, *Nature* **576**, 70 (2019).
- <sup>4</sup>R. El-Ganainy, K. G. Makris, D. N. Christodoulides, and Z. H. Musslimani, *Optics Letters* **32**, 2632 (2007).
- <sup>5</sup>K. G. Makris, R. El-Ganainy, D. N. Christodoulides, and Z. H. Musslimani, *Physical Review Letters* **100**, 103904 (2008).
- <sup>6</sup>Z. H. Musslimani, K. G. Makris, R. El-Ganainy, and D. N. Christodoulides, *Physical Review Letters* **100**, 030402 (2008).
- <sup>7</sup>A. Guo, G. J. Salamo, D. Duchesne, R. Morandotti, M. Volatier-Ravat, V. Aimez, G. A. Siviloglou, and D. N. Christodoulides, *Physical Review Letters* **103**, 093902 (2009).
- <sup>8</sup>C. E. Rüter, K. G. Makris, R. El-Ganainy, D. N. Christodoulides, M. Segev, and D. Kip, *Nature Physics* **6**, 192 (2010).
- <sup>9</sup>K. G. Makris, R. El-Ganainy, D. N. Christodoulides, and Z. H. Musslimani, *Physical Review A* **81**, 063807 (2010).
- <sup>10</sup>Y. D. Chong, L. Ge, and A. D. Stone, *Physical Review Letters* **106**, 093902 (2011).
- <sup>11</sup>P. Ambichl, K. G. Makris, L. Ge, Y. D. Chong, A. D. Stone, and S. Rotter, *Physical Review X* **3**, 041030 (2013).
- <sup>12</sup>A. Regensburger, C. Bersch, M.-A. Miri, G. Onishchukov, D. N. Christodoulides, and U. Peschel, *Nature* **488**, 167 (2012).
- <sup>13</sup>L. Feng, Y.-L. Xu, W. S. Fegadolli, M.-H. Lu, J. E. B. Oliveira, V. R. Almeida, Y.-F. Chen, and A. Scherer, *Nature Materials* **12**, 108 (2013).
- <sup>14</sup>B. Peng, S. K. Ozdemir, F. Lei, F. Monifi, M. Gianfreda, G. L. Long, S. Fan, F. Nori, C. M. Bender, and L. Yang, *Nature Physics* **10**, 394 (2014).
- <sup>15</sup>D. N. Christodoulides, F. Lederer, and Y. Silberberg, *Nature* **424**, 817 (2003).
- <sup>16</sup>D. N. Christodoulides and R. I. Joseph, *Optics Letters* **13**, 794 (1988).
- <sup>17</sup>S. M. Jensen, *IEEE Journal of Quantum Electronics* **18**, 1580 (1982).
- <sup>18</sup>N. Finlayson and G. L. Stegeman, *Applied Physics Letters* **56**, 23 (1990).
- <sup>19</sup>J. C. Eilbeck, P. S. Lomdahl, and A. C. Scott, *Physica D* **16**, 318 (1985).
- <sup>20</sup>N. Alexeeva, I. Barashenkov, K. Rayanov, and S. Flach, *Physical Review A* **89**, 013848 (2014).
- <sup>21</sup>J. Hizanidis and K. G. Makris, *Physical Review E* **110**, 064220 (2024).
- <sup>22</sup>T. Christopoulos, O. Tsilipakos, and E. E. Kriezis, *Journal of Applied Physics* **136** (2024).
- <sup>23</sup>A. Röhm, F. Böhm, and K. Lüdige, *Physical Review E* **94**, 042204 (2016).
- <sup>24</sup>G. Alfimov, P. Korchagin, and F. Abdullaev, *Chaos: An Interdisciplinary Journal of Nonlinear Science* **35** (2025).
- <sup>25</sup>V. Achilleos, G. Theocharis, and C. Skokos, *Physical Review E* **97**, 042220 (2018).
- <sup>26</sup>M. Kitano, T. Yabuzaki, and T. Ogawa, *Physical Review A* **29**, 1288 (1984).
- <sup>27</sup>G. Sivaganesh, K. Srinivasan, T. F. Fozin, and R. G. Pradeep, *Chaos, Solitons & Fractals* **174**, 113884 (2023).
- <sup>28</sup>A. Tzortzakakis, K. Makris, S. Rotter, and E. Economou, *arXiv preprint arXiv:2005.06414* (2020).
- <sup>29</sup>J. Hizanidis, N. Lazarides, and G. P. Tsironis, *Chaos: An Interdisciplinary Journal of Nonlinear Science* **30** (2020).